Magnetic ordering in magnetic shape memory alloy Ni-Mn-In-Co

K. Ollefs,[1,2,*] Ch. Schöppner,[2] I. Titov,[2,3] R. Meckenstock,[2] F. Wilhelm,[1] A. Rogalev,[1] J. Liu,[4,†] O. Gutfleisch,[4] M. Farle,[2] H. Wende,[2] and M. Acet[2]

[1]*European Synchrotron Radiation Facility (ESRF), CS 40220, F-38043 Grenoble Cedex, France*

[2]*Faculty of Physics and Center for Nanointegration Duisburg-Essen (CENIDE), Universität Duisburg-Essen, Lotharstr. 1, D-47057 Duisburg, Germany*

[3]*Faculty of Physics, M. V. Lomonosov Moscow State University, Leninskie Gory, 119991 Moscow, Russia*

[4]*Materials Science, Technische Universität Darmstadt, Alarich-Weiss-Str. 16, D-64287 Darmstadt, Germany*

(Received 23 January 2015; published 23 December 2015)

Structural and magnetic properties across the martensite-austenite phase transitions in the shape memory alloy Ni-Mn-In-Co are studied using complementary experimental techniques: ferromagnetic resonance, macroscopic magnetization measurements, and x-ray magnetic circular dichroism in the temperature range from 5 to 450 K. Ferromagnetic resonance experiments show coexisting antiferromagnetic and ferromagnetic correlations for the martensite phase and ferromagnetic and paramagnetic correlations in the austenite phase. Magnetization measurements reveal spin-glass-like behavior for $T < 30$ K and Ni and Co K-edge x-ray magnetic circular dichroism measurements confirm an assignment of a ferromagnetic resonance line purely to Ni (and Co) for a wide temperature range from 125 to 225 K. Hence a combined analysis of ferromagnetic resonance and x-ray magnetic circular dichroism allows us to attribute particular magnetic resonance signals to individual elemental species in the alloy.

DOI: 10.1103/PhysRevB.92.224429 PACS number(s): 78.70.Dm, 75.30.Sg, 76.50.+g

I. INTRODUCTION

Heusler alloys of the Ni-Mn-X family can undergo a magnetic field controlled phase transition, which leads to the ferromagnetic shape memory effect and gives rise to giant magnetoresistance [1,2], superelasticity [3,4], and magnetocaloric effects [5]. The latter, for instance, is of great technological interest due to possible exploitation as refrigerants for solid-state-cooling (see, for example, in Refs. [6,7]). These Ni-Mn-X alloys exhibit martensitic phase transitions between a ferromagnetic (FM) high-temperature phase called austenite and a low-temperature phase called martensite. The most studied magnetic shape memory alloy is Ni-Mn-Ga. However, in search of alternative memory alloys, materials with $X =$ In, Sn, or Sb have been vastly investigated. It was found that when substituting small amounts of Ni or Mn by Co in alloys with $X =$ In, Sn, or Sb, the magnetization jump at the transition enhances (favoring a large magnetocaloric effect) and the Curie temperature in the austenite phase increases [2,3,8].

The magnetic correlations in the martensite are complex, and not fully understood. A low magnetization in the martensite phase was reported for Ni-Mn-X alloys with X as In, Sn, and Sb [9,10]. These studies suggested that the magnetic interactions in this low-magnetization state were of antiferromagnetic (AF) type. Following these experiments, Mössbauer spectroscopy studies on Ni-Mn-Sn and Ni-Mn-In gave evidence that this state was paramagnetic (PM) [11,12]. However, further neutron polarization analysis studies on Ni-Mn-Sn and Ni-Mn-Sb confirmed the presence of short-range AF correlations below M_s [13]. Further ferromagnetic resonance (FMR) studies [14] have also shown that for the case of X as In, short-range AF coupling is weaker than in the case when X is Sn or Sb. The structural transition from a cubic lattice in the austenite phase to a tetragonal distorted lattice in the martensite phase is nucleation based, displacive, and diffusionless. Below the transition, the structure exhibits a lower symmetry compared to the parent cubic phase, and interatomic distances change. This has a consequence on magnetic correlations, because the magnetic interaction in the martensitic phase is due to exchange interactions between Mn atoms mediated by Ni via hybridization, where the Ni moment can be aligned ferromagnetically or antiferromagnetically depending on the next neighbors being Mn-Ni-Mn or Mn-Ni-In, respectively [15,16]. X-ray absorption studies for Ni-Mn-X have shown that the Ni moment decreases when Ga is replaced by In and even more by Sn. This is due to changes in the Ni 3d minority spin band. Mn enrichment leads to a further reduced magnetic moment on Ni atoms [15,17].

In this paper, we present a thorough investigation of the magnetic correlations in $Ni_{45}Mn_{37}In_{13}Co_5$ using the complementary techniques of FMR, magnetization measurements, and XMCD over a broad temperature range.

A. Magnetic interactions investigated by ferromagnetic resonance

Ferromagnetic resonance (FMR) is a well known technique based on the resonant absorption of microwaves in an externally applied static magnetic field $\vec{B}_{\text{ext}}$. The FMR signal thus corresponds to the imaginary part of the high-frequency magnetic susceptibility χ'' parallel to the radio frequency (rf) driving field $\vec{b}_{mw} \cdot e^{i\omega t}$, where $\vec{b}_{mw}$ is the rf magnetic field vector, and ω is the microwave frequency. In a simplified model (in a paramagnet) the condition for resonance is given by

$$\omega = \gamma B_{\text{eff}}, \tag{1}$$

*katharina.ollefs@uni-due.de

†Present address: Ningbo Institute of Materials Technology and Engineering, Chinese Academy of Sciences, 315201 Ningbo, China

where γ is the gyromagnetic ratio [18] and $B_{\text{eff}} = B_{\text{ext}} + B_{\text{internal}}$.

In this paper, we present results of FMR experiments performed at a fixed microwave frequency ω by sweeping the magnetic field. Therefore the resonance condition is determined by the applied static field $\vec{B}_{\text{ext}} = \vec{B}_{\text{res}}$.

For a paramagnet (devoid of exchange and anisotropy fields), the resonance condition is fulfilled at the resonance field

$$B_{\text{res}} = B_{\text{ext}} = B_{\text{eff}} = \frac{\omega}{\gamma} = 330\ \text{mT} \tag{2}$$

for the microwave frequency (9.2 GHz) used in the present experiments, and is an isotropic value (with $g = 2$).

For a sample with FM exchange interaction, the resonance condition becomes $B_{\text{res}} = \frac{\omega}{\gamma} - B_A$, where B_A is the anisotropy field [19]. Note that the equation is valid for the external magnetic field being oriented parallel to the symmetry axis of a uniaxial magnetic anisotropy. The resonance position is shifted to lower external field values with respect to the isotropic value. Depending on the anisotropy field, the line position can shift to higher or even lower field values in case of single-crystal samples depending on the orientation of the sample to the external field. In a sample consisting of randomly distributed crystallites like the powder sample studied here, the resonance condition is fulfilled at various external fields due to locally varying magnetocrystalline and shape anisotropy. The individual resonances merge into one broad asymmetric line. This behavior is well known for FMR measurements on nanoparticle ensembles [20].

In case of antiferromagnetic (AF) interactions, the equation for the resonance condition becomes $B_{\text{res}} = \frac{\omega}{\gamma} \mp \sqrt{B_A(2 \cdot B_E + B_A)}$ with B_E being the AF exchange field [21]. In principle, this condition is fulfilled for two different values of the external field exciting resonances either by left or by right circular polarized microwave fields. The linear polarized microwave field utilized in an FMR cavity will excite both resonances, but depending on the frequency used in the experiment, only the one at higher fields is observable if still in range of the applied external field. Coupling of AF and FM phases in addition can lead to strong exchange bias effects in the sample leading to high field resonance shifts. As can be seen from the different conditions for the resonance field B_{res}, FMR is a sensitive probe for the anisotropy fields and the nature of magnetic interactions in the sample.

B. Element-specific and orbital selective magnetic properties revealed by x-ray magnetic circular dichroism

The measurement of the x-ray absorption near the edge structure (XANES), which is defined as the x-ray absorption cross section at photon-energies up to about 30 eV higher than the absorption edge, is dominated by multiple-scattering resonances of the photoelectrons ejected at low kinetic energy and is therefore highly sensitive to the local bonding and the electronic structure of the absorbing element. XMCD is a technique measuring the difference in x-ray absorption cross-sections for right and left circular polarized x rays. For the study of complex magnetic materials, the application of XMCD is well known and established [22]. Due to the process of core-level absorption of x rays, it is element specific and orbital selective. The great advantages of XMCD are the possibilities to deduce magnetic moments both in direction and amplitude from the experimental spectra via the application of the magneto-optical sum rules [23,24]. Hence it is possible to disentangle the different contributions measured by magnetometry with element-specific information.

In the most easy way, XMCD can be understood using the two-step model in which it is a measure of the spin-polarized density of states (DOS) and the orbital moment DOS. It goes in line with a more rigorous derivation of the sum rules in a differential form [25–27], which express the x-ray absorption cross-section $\Delta\sigma$ in terms of DOS. Whenever XMCD is measured at spin-orbit-split absorption edges like the $L_{2,3}$ edges, spin and orbital contributions to the magnetic moments can be deduced. At the K edge, the core level has no spin-orbit coupling, and therefore, the angular momentum of the absorbed photon is transferred only as orbital polarization to the photo-electron. Therefore only the orbital polarization of the final states is probed [28] so that XMCD at the K edge can be expressed as

$$\begin{aligned}[\Delta\sigma_{\text{XMCD}}]_{\text{K edge}} = {} & 3C_p^D \langle l_z \rangle_p \cos(\theta)_z \\ & + \tfrac{1}{10} C_d^Q \left[\langle l_z \rangle_d + \tfrac{1}{3}(5\cos^2(\theta)_z - 3)\langle O_{zzz} \rangle_d \right] \\ & \times \cos(\theta)_z. \end{aligned} \tag{3}$$

As discussed in Ref. [29], C_p^D (C_d^Q) can be expressed in terms of the absorption cross-section per hole in the p band (d band) within the electric dipole approximation D (quadrupole approximation Q). θ_z denotes the angle between the x-ray wave vector and the magnetization direction. And $\langle l_z \rangle_{p(d)}$ represents the orbital component of the magnetized DOS with $p(d)$-like symmetry at the absorbing site. $\langle O_{zzz} \rangle_d$ is the component of an operator describing octupolar moments of orbital origin. However, it is expected to be small for cubic ligand fields [29], and we neglect it in the following. While it is not possible to obtain absolute quantitative moments directly from the XMCD at the K edge because the sum rules are not applicable in a straight forward manner [26], one can still argue that the K-edge XMCD is proportional to the magnetization of the absorbing atom.

For this experiment, we performed measurements at the K edges of Ni, Mn, and Co because, they are in the hard x-ray range with a large penetration depth (of about 5 μm) of the x rays. This in turn ensures that the measured signal is not dominated by the surface effects of the particles, but it is a measurement of the bulk properties.

II. EXPERIMENTAL DETAILS

The sample studied in this paper is a powder with the chemical composition $Ni_{45.2}Mn_{36.7}In_{13}Co_{5.1}$ (at.%). The sample was prepared by mechanically grinding melt-spun ribbons [30]. The surface velocity of the rotating copper wheel is 30 m/s. Subsequently, the sample was annealed to enhance the degree of ordering [31]. For that, the as-spun ribbons were homogenized at 1173 K for 1 h followed by water quenching. The powder sample contains single- and oligo-crystalline particles with magnetic anisotropy. However, since it has

irregular particle shapes and randomly distributed orientations, it does not exhibit magnetically preferred directions.

Magnetization measurements were performed in a Quantum Design MPMS SQUID magnetometer in a magnetic field of 5 mT and temperature range 5 K $\leqslant T \leqslant$ 380 K in a zero-field-cooled (ZFC)–field-cooled (FC)–field-warmed (FW) sequence.

For FMR investigations, the powder was sealed under argon atmosphere in a quartz tube at a pressure of 300 mbar. The FMR spectra were measured at a constant microwave frequency of 9.5 GHz sweeping the field from 1.6 to 0 T. We used a helium gas-flow cryostat for the temperature range 5 K $\leqslant T \leqslant$ 300 K and a nitrogen gas-flow cryostat for 100 K $\leqslant T \leqslant$ 450 K. The temperature variation was $\pm$0.05 K for 5 K $\leqslant T \leqslant$ 150 K and $\pm$0.1 K for 150 K $\leqslant T \leqslant$ 450 K. The FMR measurements started at 5 K in the ZFC state. The external static magnetic field was swept from 1.6 to 0 T for a complete FMR spectrum. Then, the temperature was raised to the next step at zero field, and 1.6 T was applied again for the FMR spectrum.

Since we used lock-in detection and modulated the external field, the measured resonance signal is in first order proportional to the derivative of χ'' with respect to the external field. The resonance positions are determined by a Dyson fit of the observed resonance lines as described in Ref. [32]. This Dyson lineshape takes into account the larger sample thickness compared to the microwave skin depth [33,34].

The x-ray absorption measurements were performed at beamline ID12 at the European Synchrotron Radiation Facility in Grenoble, France. Total fluorescence mode in backscattering geometry was used for detection [35]. For XAS and the corresponding XMCD measurements, a powder sample was mounted on a coldfinger of a constant flow cryostat and covered by a kapton foil of 12-μm thickness. The cryostat was inserted into the bore of a superconducting magnet. For XMCD measurements, the photon helicity was reversed after each scan of the photon-energy. To ensure that, the measured XMCD spectra are free of any experimental artifacts, the data were collected for both directions of the external magnetic field parallel and antiparallel to the incoming x-ray beam. We measured XAS and XMCD at the Ni K edge, the Mn K edge, and the Co K edge for 150 and 305 K each with an applied magnetic field of $\pm$1.6 T (matching the experimental conditions of the FMR measurements). Since the penetration depth of the x rays is smaller than the sample thickness, the recorded spectra had to be corrected for self-absorption effects. Self-absorption correction is applied by taking into account the chemical composition, density, thickness of the sample, angle of incidence of the x-ray beam, and the solid angle of the detector [36]. This approach works well in the hard x-ray energy range where the involved fluorescence channel is dominated by core atomic states of the atom.

III. RESULTS AND DISCUSSION

A. Macroscopic magnetometry

The temperature dependence of the magnetization for ZFC, FC, and FW measurements are shown in Fig. 1. After cooling the sample to 5 K, the small measuring field of 5 mT was applied, and the ZFC curve was recorded while warming the sample up to 380 K. Subsequently, the FC curve was recorded by decreasing the temperature to 5 K again, and then the FW curve was recorded by raising the temperature up to 380 K. The hysteresis between FC and FW curves is due to the structural martensitic transformation.

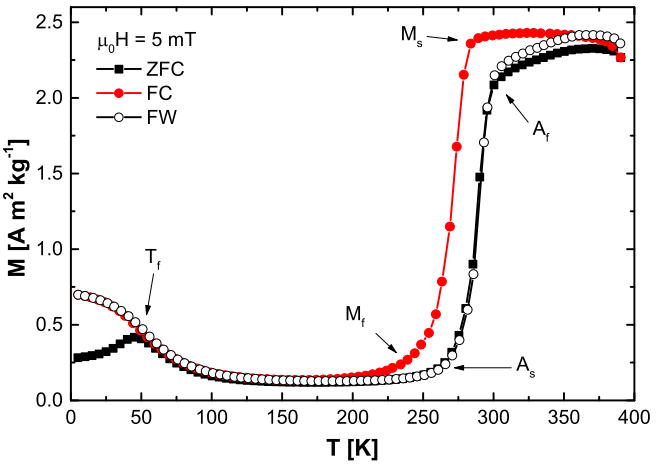

FIG. 1. (Color online) Magnetization data $M(T)$ of the powder sample $Ni_{45}Mn_{37}In_{13}Co_5$ taken at ZFC, FC and FW state in an external field of 5 mT. The initial curve is the ZFC curve.

The transition temperatures, martensite start M_s, martensite finish M_f, austenite start A_s, and austenite finish A_f are shown in Fig. 1, and the values are given in Table I.

In the austenite state above A_f and up to 380 K, the sample is FM. The Curie temperature is not within the accessible temperature range of this experiment. With decreasing temperature, the sample undergoes a martensitic transition at M_s, accompanied by a sharp decrease in the magnetization.

Below M_f, the magnetization runs nearly constant for temperatures down to 150 K. For temperatures below 150 K, the magnetization increases with decreasing temperature. For $T \leqslant$ 50 K, a separation of ZFC and FC data is present, which indicates the presence of a field and history dependent magnetic state of the sample.

As presented in the introduction, the drop in the magnetization just below M_s is known for Ni-Mn-X alloys and was discussed in terms of paramagnetism or AF correlations. For distinguishing between short-range AF coupling and paramagnetism, the comparison between Mössbauer spectroscopy [11,12] and neutron scattering [13] may not be straightforward. Although at a first glance both of these observations seem to contradict each other, they are compatible if the two different measurement techniques and their corresponding characteristic time windows are considered. A peak in the

TABLE I. Characteristic magnetic and structural transition temperatures martensite start M_s, martensite finish M_f, austenite start A_s, austenite finish A_f, and freezing temperature T_f of the powder sample $Ni_{45}Mn_{37}In_{13}Co_5$, which are marked in Fig. 1.

	M_s	M_f	A_s	A_f	T_f
Temperature (K)	285 $\pm$ 1	235 $\pm$ 1	278 $\pm$ 1	298 $\pm$ 1	50 $\pm$ 5

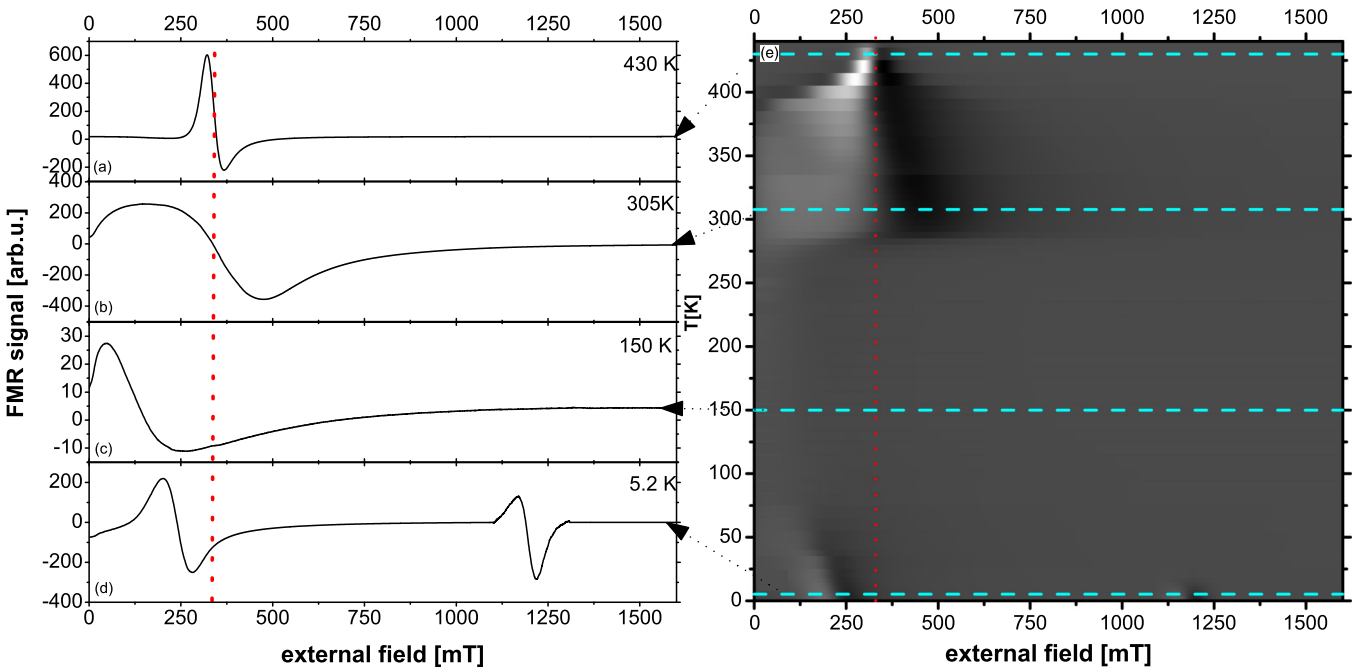

FIG. 2. (Color online) FMR experiment. (a)–(d) FMR spectra of the powder sample $Ni_{45}Mn_{37}In_{13}Co_5$ in the austenite phase at 430 K (a) and 305 K (b) and in the martensite phase at 150 K (c) and 5.2 K (d). All spectra are taken with the external field being swept from 1.6 to 0 T. (e) shows all recorded spectra for the whole temperature range in a gray-scale plot. The vertical axis represents the temperature and the horizontal axis represents the externally applied field. The intensity is color coded in gray scales. Every horizontal line is one spectrum where resonances occur at a sharp color contrast from white to black. The (red) dotted lines in each spectrum and the gray-scale plot represent the isotropic value according to Eq. (2) and the signal at higher fields is magnified by a factor of 100 for visualization.

Mössbauer spectrum can appear as single in the event of the presence of short range AF correlations and can be interpreted as a PM state. One also has to be careful when comparing the measurements on different materials because the magnetic interactions can indeed vary significantly. However, it is unlikely to have a fully disordered PM state in the martensite temperature range in the materials studied, since the martensite state occurs below the austenite state where long range FM arrangement is found. Since the present sample also shows low magnetization in a broad temperature range in the martensite state, we investigated the magnetic interactions in this particular temperature range with additional FMR and XMCD measurements, which will be discussed in the following sections.

The separation below 50 K could be caused by the presence of spin-glass-like frustration. In the case of Mn-rich alloys, as the studied sample, the martensitic structure leads to different Mn-Mn spacings within the lattice with Mn atoms being nearest neighbors along [110] directions. Hence competing FM and AF interactions are possible between Mn atoms depending on whether they occupy Mn (Mn_{Mn}) or In (Mn_{In}) sites. This leads to a frustrated spin configuration when the sample is cooled through the freezing temperature T_f. From the $M(T)$ data in Fig. 1, T_f can be estimated to be 50 K at 5 mT. At this point, the splitting of ZFC and FC curves vanishes with increasing temperature. Increasing temperature leads to the reverse martensitic transition to the austenite phase from A_s to A_f. To gain further insight into the magnetic interactions, we discuss the results of temperature dependent FMR, x-ray absorption spectroscopy (XAS) and XMCD investigations.

B. Ferromagnetic resonance

In Figs. 2(d) and 2(c), we show FMR spectra in the martensite phase at 5.2 and 150 K, respectively. The dashed red line indicates the isotropic value, according to Eq. (2). For 5.2 K, the spectrum shows two well defined resonance lines with resonance fields 240 and 1200 mT. Note that the signal at higher fields is magnified by a factor of 100 for better visualization. Following the resonance conditions mentioned in Sec. I, these two signals can be attributed to different magnetic interactions within the sample at 5.2 K. The resonance at 240 mT is due to FM interactions, while the one at 1200 mT is due to AF interactions [14,37]. Since the intensity of an FMR resonance signal is proportional to the number of magnetic moments being involved in the excited precession, the large difference in intensity between the two signals implies that more moments are coupled ferromagnetically than antiferromagnetically. Taking into account the relatively low resonance field of 1200 mT for an antiferromagnet, we conclude that only weak AF coupling is present in this sample. This coupling is superexchange mediated by Ni atoms for Mn-Ni-In configurational sequences [15]. This weak AF coupling is the cause for the ZFC-FC-splitting observed in $M(T)$ and gives rise to a frustrated spin configuration at low temperatures. From the $M(T)$ data in Fig. 1, a critical temperature for the onset of AF coupling can be estimated to be $T_0 = 50$ K under 5 mT. The critical temperature for the appearance of the resonance line involving AF interactions in the FMR experiment is also similar as can be seen in Fig. 2(e). This figure shows the complete temperature dependent FMR results on a grayscale plot. Here, the vertical

axis represents the static magnetic field and the horizontal axis represents the temperature. Every vertical line represents one FMR spectrum. Resonance positions are indicated by a sharp color change from white to black and additional colored symbols. For temperatures $T \leqslant 20$ K, a resonance related to AF interactions is observed in the high field range above 1000 mT. The intensity of the line decreases with increasing temperature until it fully vanishes at 23 K. With this, magnetization and FMR experiments clearly show a mixed FM and AF state in NiMnInCo for the martensite phase in the temperature range for 5 K $\leqslant T \leqslant$ 50 K. We attribute the FM coupling to the majority of Mn atoms for which the d-states hybridize with those of Ni atoms in Mn-Ni-Mn configurational sequences [38].

The FMR signal at 5.2 K shown in the spectrum in Fig. 2(d) can be clearly observed up to 35 K in the gray scale plot in Fig. 2(e) as well. The loss of intensity is almost as drastic as in the AF line and goes along with a downshift of the resonance position to 130 mT. This low intensity resonance is shown in the spectrum at 150 K in Fig. 2(c). It shows only 10% of the intensity of the resonance line at 5.2 K. We attribute both effects, the intensity loss and the downshift of the resonance line, to a weakening of FM correlations between the Mn atoms. The remaining FMR signal is observed for temperatures up to the structural phase transition at 280 K and shows that the martensite phase of NiMnInCo is FM at all temperatures. Since the magnetic moment of Ni is estimated to be about 5%–10% of the Mn magnetic moment in these alloys [15,17], and assuming Co carries, a moment similar to that of Ni, the FMR line should be due to the Ni and Co atoms. The asymmetry in the FMR line could therefore be due to the overlap of individual Ni and Co resonance lines. This hypothesis will be addressed using the element specific XMCD tool and is discussed in the following chapter.

Along with the structural phase transition to the austenite state starting at 278 K, the FMR spectra change again in two ways. The intensity of the resonance line increases, and the resonance position shifts upwards again. Figure 2(b) shows a recorded FMR spectrum at 305 K, above A_f, and within the temperature range of the $M(T)$ data. The resonance field is about 330 mT, while the line shows strong asymmetric features, which we attribute to an overlap of many resonance lines occurring at different resonance positions in the range from 100 to 400 mT. In a powder sample with randomly distributed anisotropy axes over the sample volume, an effective anisotropy field determines the FMR with a broadening of the line width and an asymmetric line shape as discussed in Sec. I.

Figure 2(a) shows the FMR spectrum at 430 K. The narrow resonance line at the isotropic value is a PM resonance line at $T > T_C$ for the austenite phase. This line is slightly asymmetric as well, which we attribute to the fact that the thickness of the sample is larger than the skin depth of the microwave [18]. From Fig. 2(e), we can estimate T_C of the austenite phase to 410–420 K from the FMR spectra. This value is in good agreement with the T_C found for a similar composition [39]. However, small deviations in composition can lead to some deviations in T_C [40].

C. XAS and XMCD

The x-ray absorption near the edge structure (XANES) and XMCD spectra were recorded at 150 K in the martensitic phase in order to complement the FMR measurement in Fig. 2(c) and the region of low magnetization in Fig. 1. They were also recorded at 305 K in the austenite phase to augment the FMR data in Fig. 2(b) and the region of saturation for the FC curve in Fig. 1.

Figure 3 summarizes the results of the XMCD and XANES measurements. In the upper panel, the K-edge XANES spectra are shown for both temperatures for Mn (a), Co (c), and Ni (e), respectively. In the lower panel, the corresponding XMCD spectra are depicted for Mn (b), Co (d), and Ni (f). Since only 5 at.% Co is incorporated in the sample, the signal to noise ratio for Co is smaller than that for Ni.

For all three constituents, the XANES shows significant changes comparing the low- and high-temperature data in Figs. 3(a), 3(c), and 3(e). This reflects the change in the local surrounding of all three elements due to the martensitic transformation from a tetragonally distorted structure at 150 K to a cubic phase at 305 K. The shape of the rising edge of the absorption, however, remains largely unchanged by the transformation indicating an unchanged local electronic structure of atoms.

As described in Sec. I and using Eq. (3), the XMCD measured at the K edges reflects the orbital component of the DOS of p- and d-like symmetry and its intensity is proportional to the total magnetization of the atom. The results are discussed qualitatively with respect to the FMR results.

The XMCD spectra shown in Figs. 3(b), 3(d), and 3(f) show a clear XMCD signal for all constituents in the austenite phase at 305 K. The XMCD signal is dominantly visible in the rising edge of the absorption and not at the maximum of the absorption edges. The absorption signal at the rising edge could be assigned to quadrupolar $1s \rightarrow 3d$ transitions. The spectral shape is therefore very different from the one of metallic Ni [41], Co [42], and MnAs [43]. This has been also observed for the Ni XMCD in a NiMnGa alloy [44,45] (note the inverse sign in Ref. [45]) and was attributed to a relative change in Fermi energy in this alloy with respect to pure Ni metal by comparison with calculated spectra. The sign and shape of the XMCD is similar to the one measured for the ferromagnet $TbNi_5$ [46] and therefore indicates a parallel alignment of Mn and Ni (and Co) moments. While these findings are corroborating our FMR results they are in contrast to the results of XMCD measurements at the L edges in thin films where anti-parallel alignment of the Mn and Ni(Co) moments was found [47]. These different findings can result from the fact that for the Ni (and Co) L edges surface effects can be dominant.

In our measurements for Ni and Co, the XMCD is of similar shape reflecting a similar polarization of p (d) orbitals for both elements. This is expected since they occupy the same lattice sites.

In the low-temperature phase, Mn shows no XMCD signal, while for Ni, a small XMCD is observed although the signal to noise ratio is increased here (and for Co the XMCD signal is hidden in the noise level of the measurements). Therefore a small magnetic moment can be attributed to Ni (and is not

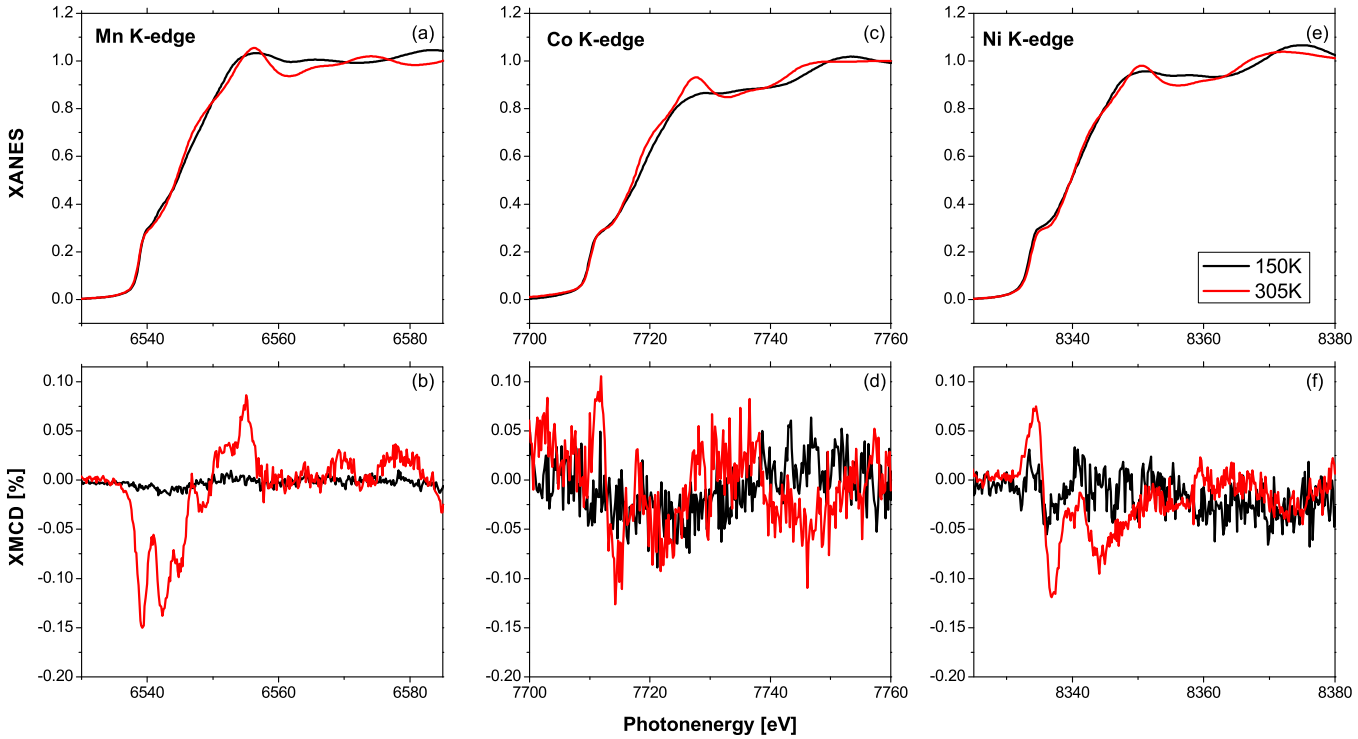

FIG. 3. (Color online) XANES (top) and XMCD (bottom) spectra for the powder sample $Ni_{45}Mn_{37}In_{13}Co_5$ recorded at the Mn [(a) and (b)], Co [(c) and (d)], and Ni [(e) and (f)] K edges. The spectra were recorded at 105 K (in black) and at 305 K (in red).

excluded for Co) in the martensite phase at 150 K, and the weak FMR line observed in this temperature regime can be assigned to the Ni (and Co) atoms in the alloy.

IV. CONCLUSION

We have investigated magnetic correlations in the shape memory alloy Ni-Mn-In-Co by means of temperature dependent FMR, SQUID, and XMCD in the range from 5 to 450 K covering magnetic and structural transitions. We find a mixed AF and FM phase for low temperatures up to a critical temperature of about 50 K in the FMR experiment. This is attributed to a spin-glass-like behavior of frustrated magnetic moments of the Mn atoms which is supported by $M(T)$ data. For higher temperatures within the martensite phase, we find weak but clear ferromagnetism from the FMR experiment. This is attributed to Ni (and Co) atoms in the alloy, proven by XMCD measurements at 150 K. The martensitic transition can be followed by the change of the FMR line position and shape, which reflects the FM austenite phase with magnetic anisotropy. The absence of weak AF interactions in the results of the present experiments and observed in Ni-Mn-In [14] is expected to be due to the Co in the sample which enhances FM exchange. The enhanced FM exchange is also expected to affect the Mn-Mn coupling so that anti-ferromagnetism is weakened, and in fact, the Mn-Mn coupling can become weakly ferromagnetic. The absence of a significant FM or AF Mn contribution is in line with earlier discussions related to bandstructure considerations [40]. Ni, Mn and Co show clear XMCD signals for the austenite phase. The FMR experiment gives $T_C = 410$–420 K and clear PM resonance lines for $T > T_C$ with asymmetric line shapes due to the thickness of the sample.

ACKNOWLEDGMENT

This work was supported by Deutsche Forschungsgemeinschaft via priority program SPP1599.

[1] K. Koyama, H. Okada, K. Watanabe, T. Kanomata, R. Kainuma, W. Ito, K. Oikawa, and K. Ishida, Appl. Phys. Lett. **89**, 182510 (2006).

[2] S. Y. Yu, L. Ma, G. Liu, Z. Liu, J. Cheng, Z. Cao, G. Wu, B. Zhang, and X. X. Zhang, Appl. Phys. Lett. **90**, 242501 (2007).

[3] R. Kainuma, Y. Imano, W. Ito, Y. Sutou, H. Morito, S. Okamoto, O. Kitakami, K. Oikawa, A. Fujita, T. Kanomata, and K. Ishida, Nature (London) **439**, 957 (2006).

[4] T. Krenke, E. Duman, M. Acet, E. F. Wassermann, X. Moya, L. Manõsa, A. Planes, E. Suard, and B. Ouladdiaf, Phys. Rev. B **75**, 104414 (2007).

[5] T. Krenke, E. Duman, M. Acet, E. F. Wassermann, X. Moya, L. Manñosa, and A. Planes, Nat. Mater. **4**, 450 (2005).

[6] S. Fähler, U. K. Rößler, O. Kastner, J. Eckert, G. Eggeler, H. Emmerich, P. Entel, S. Müller, E. Quandt, and K. Albe, Adv. Eng. Mater. **14**, 10 (2012).

[7] J. Liu, T. Gottschall, K. P. Skokov, J. D. Moore, and O. Gutfleisch, Nat. Mater. **11**, 620 (2012).

[8] A. K. Nayak, K. G. Suresh, and A. K. Nigam, J. Phys. D: Appl. Phys. **42**, 035009 (2009).

[9] T. Krenke, M. Acet, E. F. Wassermann, X. Moya, L. Mañosa, and A. Planes, Phys. Rev. B **72**, 014412 (2005).

[10] T. Krenke, M. Acet, E. F. Wassermann, X. Moya, L. Mañosa, and A. Planes, Phys. Rev. B **73**, 174413 (2006).

[11] R. Y. Umetsu, R. Kainuma, Amako Y. Taniguchi, T. Kanomata, K. Fukushima, A. Fujita, K. Oikawa, and K. Ishida, Appl. Phys. Lett. **93**, 042509 (2008).

[12] V. V. Khovaylo, T. Kanomata, T. Tanaka, M. Nakashima, Y. Amako, R. Kainuma, R. Y. Umetsu, H. Morito, and H. Miki, Phys. Rev. B **80**, 144409 (2009).

[13] S. Aksoy, M. Acet, P. P. Deen, L. Mañosa, and A. Planes, Phys. Rev. B **79**, 212401 (2009).

[14] S. Aksoy, O. Posth, M. Acet, R. Meckenstock, J. Lindner, M. Farle, and E. F. Wassermann, J. Phys.: Conf. Ser. **200**, 092001 (2010).

[15] K. R. Priolkar, P. A. Bhobe, D. N. Lobo, S. W. D'Souza, S. R. Barman, A. Chakrabarti, and S. Emura, Phys. Rev. B **87**, 144412 (2013).

[16] J. Enkovaara, O. Heczko, A. Ayuela, and R. M. Nieminen, Phys. Rev. B **67**, 212405 (2003).

[17] S. Imada, A. Yamasaki, T. Kanomata, T. Muro, A. Sekiyama, and S. Suga, J. Magn. Magn. Mater. **310**, 1857 (2007).

[18] C. Poole, *Electron Spin Resonance* (MacGraw Hill, New York, 1967).

[19] C. Kittel, Phys. Rev. **73**, 155 (1948).

[20] A. Trunova, R. Meckenstock, I. Barsukov, C. Hassel, O. Margeat, M. Spasova, J. Lindner, and M. Farle, J. Appl. Phys. **104**, 093904 (2008).

[21] C. Kittel, Phys. Rev. **82**, 565 (1951).

[22] G. van der Laan and A. Figueroa, Coord. Chem. Rev. **277**, 95 (2014).

[23] B. T. Thole, P. Carra, F. Sette, and G. van der Laan, Phys. Rev. Lett. **68**, 1943 (1992).

[24] P. Carra, B. T. Thole, M. Altarelli, and X. Wang, Phys. Rev. Lett. **70**, 694 (1993).

[25] P. Strange, J. Phys.: Condens. Matter **6**, L491 (1994).

[26] G. Y. Guo, J. Phys.: Condens. Matter **8**, L747 (1996).

[27] H. Ebert, V. Popescu, and D. Ahlers, Phys. Rev. B **60**, 7156 (1999).

[28] J. I. Igarashi and K. Hirai, Phys. Rev. B **50**, 17820 (1994).

[29] A. Rogalev, J. Goulon, F. Wilhelm, Ch. Brouder, A. Yaresko, J. Ben Youssef, M. V. Indenbom, J. Magn. Magn. Mater. **321**, 3945 (2009).

[30] J. Liu, N. Scheerbaum, S. Weiss, and O. Gutfleisch, Appl. Phys. Lett. **95**, 152503 (2009).

[31] J. Liu, T. G. Woodcock, N. Scheerbaum, and O. Gutfleisch, Acta Mater. **57**, 4911 (2009).

[32] B. Emre, S. Aksoy, O. Posth, M. Acet, E. Duman, J. Lindner, and Y. Elerman, Phys. Rev. B **78**, 144408 (2008).

[33] F. J. Dyson, Phys. Rev. **98**, 349 (1955).

[34] G. Feher and A. F. Kip, Phys. Rev. **98**, 337 (1955).

[35] A. Rogalev, J. Goulon, C. Goulon-Ginet, and C. Malgrange, Lect. Notes Phys. **697**, 71 (2001).

[36] F. Wilhelm, N. Jaouen, A. Rogalev, W. G. Stirling, R. Springell, S. W. Zochowski, A. M. Beesley, S. D. Brown, M. F. Thomas, G. H. Lander, S. Langridge, R. C. C. Ward, and M. R. Wells, Phys. Rev. B **76**, 024425 (2007).

[37] M. Hagiwaray, K. Katsumatay, I. Yamadaz, and H. Suzuki, J. Phys.: Condens. Matter **8**, 7349 (1996).

[38] K. R. Priolkar, D. N. Lobo, P. A. Bhobe, S. Emura, and A. K. Nigam, Europhys. Lett. **94**, 38006 (2011).

[39] F. Guillou, P. Courtois, L. Porcar, P. Plaindoux, D. Bourgault, and V. Hardy, J. Phys. D: Appl. Phys. **45**, 255001 (2012).

[40] A. N. Vasiliev, O. Heczko, O. S. Volkova, T. N. Vasilchikova, T. N. Voloshok, K. V. Klimov, W. Ito, R. Kainuma, K. Ishida, K. Oikawa, and S. Fähler, J. Phys. D: Appl. Phys. **43**, 055004 (2010).

[41] R. Torchio, Y. O. Kvashnin, S. Pascarelli, O. Mathon, C. Marini, L. Genovese, P. Bruno, G. Garbarino, A. Dewaele, F. Occelli, and P. Loubeyre, Phys. Rev. Lett. **107**, 237202 (2011).

[42] A. Ney, M. Opel, T. C. Kaspar, V. Ney, S. Ye, K. Ollefs, T. Kammermeier, S. Bauer, K.-W. Nielsen, S. T. B. Goennenwein, M. H. Engelhard, S. Zhou, K. Potzger, J. Simon, W. Mader, S. M. Heald, J. C. Cezar, F. Wilhelm, A. Rogalev, R. Gross, and S. A. Chambers, New J. Phys. **12**, 013020 (2010).

[43] P. Wadley, A. A. Freeman, K. W. Edmonds, G. van der Laan, J. S. Chauhan, R. P. Campion, A. W. Rushforth, B. L. Gallagher, C. T. Foxon, F. Wilhelm, A. G. Smekhova, and A. Rogalev, Phys. Rev. B **81**, 235208 (2010).

[44] J. Chaboy, P. Lázpita, J. M. Barandiarán, J. Gutiérrez, M. L. Fernández-Gubieda, and N. Kawamura, J. Phys.: Condens. Matter **21**, 016002 (2009).

[45] Z. Islam, D. Haskel, J. C. Lang, G. Srajer, Y. Lee, B. N. Harmon, A. I. Goldman, D. L. Schlagel, and T. A. Lograsso, J. Magn. Magn. Mater. **303**, 20 (2006).

[46] R. M. Galéra and A. Rogalev, J. Appl. Phys. **85**, 4889 (1999).

[47] P. Klaer, H. C. Herper, P. Entel, R. Niemann, L. Schultz, S. Fähler, and H. J. Elmers, Phys. Rev. B **88**, 174414 (2013).